Laser Processing of Dissimilar Metals

G.Phanikumar, P.Dutta* and K.Chattopadhyay
Department of Metallurgy, *Department of Mechanical Engineering
Indian Institute of Science, Bangalore 560012

Abstract

The paper summarises the work carried out at the Indian Institute of Science in recent time on Laser processing of dissimilar materials in welding and surface alloying configurations for various model metallurgical systems. The microstructural features observed in the systems studied are summarized. A three dimensional transient computational model, to solve heat transfer, fluid flow and species conservation equations, is developed to simulate the processes. Salient features of the computational results are presented.

1. Introduction

Laser welding has been studied well for various metals and alloys in different configurations [1,2]. An understanding of the physical processes that take place during welding that effect the weld material properties exists. However, laser welding of dissimilar metals has not been studied in detail in the literature [3,4]. Majority of this literature is mainly concentrated on the joining of dissimilar steels and deal with the analysis of the problem in a case-by-case manner. From the scientific standpoint, analysis of a dissimilar metal joint offers a number of challenges arising out of complexities such as dissimilar metal properties, asymmetric weld pool shape, mixing of the molten metals, segregation, and formation of intermetallic compounds. We are carrying out a comprehensive programme of research at the Indian Institute of science to address some of these issues. In the present paper, we shall review some of the progress that has been made by us in this direction.

Mathematical modeling and simulation have been used to gain insight into the physical processes that occur in a weld pool [5,6], as it is very difficult to make a direct observation of the weld pool solidification behavior [7]. Literature shows a good success in computer simulation of autogenous welding of metals [8] but almost no literature exists on the simulation of dissimilar welding till now [9,10]. We have made a preliminary attempt to simulate dissimilar welding for the first time. In spite of a large number of assumptions made in the work, we have found that a good insight could be developed for understanding the physical processes that take place in dissimilar welding.

The choice of laser as heat source is made as it is devoid of any chemical contamination or magnetic effects. The simplicity of the heat source also eases analysis of welds and computational modeling to gain insights. Additionally, high processing rates are possible since there is no inertia associated with the coupling of laser heat with the metal.

2. Welding Experiments

A schematic of the laser welding setup is shown in Fig. 1a. Laser welding involves high cooling rates and temperature gradients leading to a high rate of solidification. Metastable microstructure formation and non-equilibrium effects have been observed. In the present review, we shall present results on those binary metallic systems where intermetallic compound

formation is not present to maker the process of analysis easier. Three systems have been chosen for study, namely, copper-nickel, copper-iron and iron-nickel that will be referred to as A-B couples. Copper-nickel system has an isomorphous phase diagram, iron-copper system is an immiscible system and iron-nickel system has a wide solid-solution formation and a Fe_3Ni phase formation. One can see that an analysis of these three systems could give an insight in to the physical processes that take place during laser welding of model dissimilar metal couples.

Commercial high purity metals are taken in the form of bars of square cross section of 7mm × 7mm each and are fixed on a CNC table in butt-weld geometry. Continuous wave CO_2 laser is used as the heat source at powers of around 5 kW at various scan speeds. Laser diameter is 0.5 mm. A gas shroud of 30%He + 50%Ar is used to prevent the liquid metal from contact with atmosphere. Table-1 shows a list of parameters used for the three systems [11]. Weld samples are cut to make transverse sections for characterization using optical microscopy, scanning electron microscopy (SEM) and composition analysis using EDAX.

2.1 Experimental Results:

Microstructural features of the three systems showed similar features though they are metallurgically different. Typical weld microstructures of the three systems are shown in the Fig. 2. It is observed that at low scan speeds the weld pool is narrow and deep with keyhole formation. A minimal amount of porosity is also noticed. The microstructure reveals segregation patterns that are asymmetric in nature. At high scan speed, the 'eye' of the pattern lies on B-side and at low scan speed, there is one 'eye' towards the top and one towards the bottom. The extent of melting itself is found asymmetric; with more melting on B-side, though the laser heat source has been placed symmetrically over the joint A-B.

Microstructural features are also seen to be asymmetric. B-weld interface is sharp and shows a continuous growth of the base metal in to the weld (Fig. 3). Weld microstructure near the interface also shows bands. The microstructure of the A-side interface, on the other hand, is very jagged showing that growth of solid into the weld is not as straight forward as in the case of B-side. On the A-side, we notice the interface to be rough with swirls of A-rich and B-rich regions in an irregular pattern (Fig. 4). The weld pool microstructure consists of irregular bands within which cells can be resolved. The cells from one band often do not extend to the other band.

The microstructure throughout the weld exhibits a cellular/dendritic structure. Extensive microstructural banding, compositional fluctuations and irregularity of the microstructural features on A-side are very distinct for all scan speeds. Microstructural bands comprise of a change in the scale of microstructure as well as fluctuations in the composition. EDAX analysis across a set of bands showed a fluctuation of the composition. The shapes of bands and composition variations suggest a discontinuous growth of the solid-liquid interface in the weld pool.

2.2 Discussion:

As the scan speed is decreased, the change in weld pool shape can be attributed to a change in the welding mode from 'conduction' to 'keyhole'. This kind of a transition in the welding mode is well documented in the literature [12] as due to the formation of vapor and the subsequent enhancement in the efficiency of absorption of radiation leading to deep penetration. Side-B has lower thermal diffusivity compared to side-A. Side-B can thus have more sensible heat than side-A and its rise in temperature is expected to be faster. This more than compensates the higher melting point of side-B and leads to extended melting in comparison to side-A leading to a shift of weld pool towards side-B.

Side-B is thus, expected to melt first and the high temperature gradient on the surface of the melt should give rise to surface tension gradient driven flow that leads to the convection in the melt. Heat transport from the top of the melt to the lower portions to melt the base metal and the final shape of the weld pool, are dictated predominantly by this process. The simulation results presented in the next section give more insight in to this issue.

We observe that the microstructural features discussed above are common to several other dissimilar couples including Al-Ni [13], Al-Ti [14], and Ti-Ni[15], where the low melting side has the complex mixing patterns and the high melting side has a smooth interface. At this point, we can only say that the complex patterns could be due to one of the following two reasons: Double diffusive / complex convection patterns near the interface that are frozen in to the weld before complete development. Alternately, a combination of mixing and remelting processes take place at the interface and led to the formation of such patterns.

3. Computational modeling of dissimilar welding

A full scale modeling of a moving dissimilar weld pool (i.e. produced by a continuous laser welding) requires modeling of the melting, mixing and solidification at both micro and macro scales. Solidification modeling in such a situation is a very difficult task, since the composition can vary sharply at any location. In addition, the solidification process would depend on the scale of mixing of the two metals at the interface, which may be very difficult to determine using present modeling tools [16]. In the case of a stationary spot weld, however, we can have a distinct process of melting during the application of the laser, followed by a solidification process after the laser is switched off (assuming no remelting). Since the melting process involves only pure metals (initially separated in a butt welding arrangement), we have the option to model it without having to consider the solidification process. It may be noted that any mixing of metals due to convection occurs only after the material is molten. In the present case we attempt to model the melting and mixing processes at a macroscopic level by considering a stationary-welding situation of a copper-nickel couple. The objective is to study the asymmetry of a weld pool caused by a symmetric heat source on a dissimilar metal joint and the associated temperature, velocity and mass fraction distributions.

The copper nickel system chosen is very close to an ideal binary system with complete miscibility in liquid and solid states, and hence it justifies most of the assumptions we have made with regard to our mixture model. One important property that is very difficult to estimate for the simulation is the efficiency of absorption of heat from the laser beam. While the surface finish and emissivity reduce the coupling efficiency, vapor and plasma formation on the surface of melt enhance the same. It is very difficult to get the coupling efficiency from the experiment and published literature on this issue is not adequate. We use a constant emissivity through out the temperature range. We choose the effective coupling efficiency such that the computed weld pool is as wide as the experimentally observed one, keeping all other welding parameters same. Once the efficiency is calibrated, all data that can be extracted from the simulation is used to compare our calculations with the experiments. Further, it should be noted that the weld pool shape and qualitative details will be unaffected by small changes in the coupling efficiency and a quantitative agreement is not aimed at in this preliminary modeling attempt.

In the welding of dissimilar metals, the two metals melt and mix in the weld pool. For our simulation, we consider a locally homogeneous model where flow is characterized by the properties assigned according to the relative proportion of each phase in the mixture. Correlations are required to provide estimates of properties in relevant flow regimes. Although some information regarding interface related quantities will be lost by assuming a homogeneous model, the present study may still give some insight into this complex problem with regard to flow field, asymmetry of pool shape, temperature field, and mixing.

3.1 Mathematical Formulation:

A schematic of the computational domain used for numerical simulation is shown in Fig 1a. Two pieces of copper and nickel with equal dimensions are kept in a butt joint. A Gaussian heat input is applied from the top at the centerline of the butt joint such that the heat is distributed equally on both pieces. The fluid motion in the melt pool is assumed to be laminar and incompressible, and the system is in unsteady state. The top surface after melting is assumed flat. Variation of density has been considered only in the body force term of the momentum equation (Boussinesq approximation). Thermophysical properties are taken to be different for solid and liquid metals, and variation with temperature taken in to consideration using a smooth fit over the data available at different temperatures in the literature [11]. For properties of the mixtures, semi-empirical correlations are used. Thermal conductivity, specific heat, density, viscosity, and surface tension are considered as functions of temperature and mass fraction.

Phase change is modeled using an enthalpy-porosity technique [17,18]. As discussed earlier, only melting of pure metals need to be considered if we are modeling the melting phenomenon in a stationary spot weld. For a given control volume, pure metal properties (including latent heat of fusion) are used until melting takes place. Once melting occurs followed by mixing and transport of material from the other metal, mixture rules for the properties are applied.

The resulting governing equations for mass, momentum, energy and species equations are as follows:

Continuity:

$$\frac{\partial \rho}{\partial t} + \frac{\partial}{\partial x}(\rho u) + \frac{\partial}{\partial y}(\rho v) + \frac{\partial}{\partial z}(\rho w) = 0 \qquad [1]$$

Momentum:

$$\frac{\partial}{\partial t}(\rho u) + \frac{\partial}{\partial x}(\rho u u) + \frac{\partial}{\partial y}(\rho v u) + \frac{\partial}{\partial z}(\rho w u) = \frac{\partial}{\partial x}\left(\mu \frac{\partial u}{\partial x}\right) + \frac{\partial}{\partial y}\left(\mu \frac{\partial u}{\partial y}\right) + \frac{\partial}{\partial z}\left(\mu \frac{\partial u}{\partial z}\right) - \frac{\partial p}{\partial x} + S_x \qquad [2]$$

$$\frac{\partial}{\partial t}(\rho v) + \frac{\partial}{\partial x}(\rho u v) + \frac{\partial}{\partial y}(\rho v v) + \frac{\partial}{\partial z}(\rho w v) = \frac{\partial}{\partial x}\left(\mu \frac{\partial v}{\partial x}\right) + \frac{\partial}{\partial y}\left(\mu \frac{\partial v}{\partial y}\right) + \frac{\partial}{\partial z}\left(\mu \frac{\partial v}{\partial z}\right) - \frac{\partial p}{\partial y} + S_y \qquad [3]$$

$$\frac{\partial}{\partial t}(\rho w) + \frac{\partial}{\partial x}(\rho u w) + \frac{\partial}{\partial y}(\rho v w) + \frac{\partial}{\partial z}(\rho w w) = \frac{\partial}{\partial x}\left(\mu \frac{\partial w}{\partial x}\right) + \frac{\partial}{\partial y}\left(\mu \frac{\partial w}{\partial y}\right) + \frac{\partial}{\partial z}\left(\mu \frac{\partial w}{\partial z}\right) - \frac{\partial p}{\partial z} + S_z \qquad [4]$$

Energy:

$$\frac{\partial}{\partial t}(\rho H) + \frac{\partial}{\partial x}(\rho u H) + \frac{\partial}{\partial y}(\rho v H) + \frac{\partial}{\partial z}(\rho w H) = \frac{\partial}{\partial x}\left(k \frac{\partial T}{\partial x}\right) + \frac{\partial}{\partial y}\left(k \frac{\partial T}{\partial y}\right) + \frac{\partial}{\partial z}\left(k \frac{\partial T}{\partial z}\right) + S_h \qquad [5]$$

Mass fraction:

$$\frac{\partial C}{\partial t}+\frac{\partial}{\partial x}(uC)+\frac{\partial}{\partial y}(vC)+\frac{\partial}{\partial z}(wC)= \frac{\partial}{\partial x}\left(D_{AB}\frac{\partial C}{\partial x}\right)+\frac{\partial}{\partial y}\left(D_{AB}\frac{\partial C}{\partial y}\right)+\frac{\partial}{\partial z}\left(D_{AB}\frac{\partial C}{\partial z}\right) \quad [6]$$

The above source terms according to our enthalpy-porosity formulation are expressed as follows:

$$S_x=-\left(\frac{K(1-\varepsilon)^2}{\varepsilon^3+b}\right)u \quad [7]$$

$$S_y=-\left(\frac{K(1-\varepsilon)^2}{\varepsilon^3+b}\right)v+\rho g[\beta_T(T-T_r)-\beta_C(C-C_r)] \quad [8]$$

$$S_z=-\left(\frac{K(1-\varepsilon)^2}{\varepsilon^3+b}\right)w \quad [9]$$

$$S_h=-\frac{\partial}{\partial t}(\rho\Delta H) \quad [10]$$

Where K is a morphological constant, b is an arbitrary small number to prevent division by zero, ΔH is the latent heat content of a control volume, and ε is the liquid fraction calculated as $\frac{\Delta H}{L}$, with L being the latent heat of melting for the corresponding metal.

Boundary and initial conditions: At time $t=0$, the entire domain is in the solid state at room temperature. At time $t>0$, the following boundary conditions are applied:
At the top surface of the work piece, a heat flux with a Gaussian distribution is applied, as given by:

$$q''(r)=\frac{\eta Q}{\pi r_q^2}\exp\left(-\frac{r^2}{r_q^2}\right) \quad [11]$$

At the flat free surface of the liquid, shear force due to surface tension is expressed as:

$$\mu\left.\frac{\partial u}{\partial y}\right|_{y=h}=\sigma_T\left.\frac{\partial T}{\partial x}\right|_{y=h}+\sigma_C\left.\frac{\partial C}{\partial x}\right|_{y=h} \quad [12]$$

$$\mu\left.\frac{\partial w}{\partial y}\right|_{y=h}=\sigma_T\left.\frac{\partial T}{\partial z}\right|_{y=h}+\sigma_C\left.\frac{\partial C}{\partial z}\right|_{y=h} \quad [13]$$

Also, no mass transfer is considered at the top surface. The bottom surface is insulated, while the four sides are subjected to convective and radiative heat loss.

3.2 Numerical Procedure:

The three-dimensional coupled continuity, momentum, energy, and mass fraction equations along with the boundary conditions are solved numerically using a finite volume technique. The general framework of the numerical solution rests on SIMPLER algorithm [19], modified appropriately to accommodate phase change processes and mixing of dissimilar metals.

Transient studies are carried out until some mixing patterns are obtained. The thermophysical data for the case study is given in table-2. A non-uniform grid of 64×48×64 is used to discretize the computational domain, with a high concentration of grids inside the weld pool.

3.3 Discussion of Computational Results:

Due to the difference in thermal diffusivity of copper and nickel, heat diffusion in copper will be more than in nickel during the conduction phase of the heating process. Nickel, which has a lower thermal conductivity, will be experiencing a temperature rise faster than copper. Consequently, the location of maximum temperature will be shifted towards the nickel side. Depending on the rate of heating of the two metals and their respective melting points, we can expect either of the two metals to melt first. In the present case, the low thermal conductivity of nickel more than compensates for its high melting point and melts first.

After nickel starts melting, the weld pool develops a flow starting from the maximum temperature location and moves outwards. Since the temperature coefficient of the surface tension, σ_t, is negative, the value of the surface tension at the maximum temperature location is lower than that at the edges of the weld pool. Hence, the fluid in the center is pulled radially outward. From Fig. 5 and 6, it can be seen that due to asymmetric heating and convection, isotherms bend and become non-circular. On the free surface, convection brings the hot liquid from the maximum temperature location to the edges of the weld pool, thus increasing the width of the weld pool. By continuity, this flow also brings the cold fluid from the bottom of the pool to the surface. The amount of heat transported in the vertical direction is therefore relatively small. Hence, the melt pool tends to be shallow and wide. Since surface tension forces are dominant, the maximum velocity occurs on the free surface. The eye of the convection cell is close to the surface.

Figure 7 shows a top view of the evolution of heating and weld pool formation. It is observed that the nickel side melts first and subsequently convection carries the heat towards the copper side. Thus, the rise in temperature and melting of the copper side is aided by convection from the nickel side, in addition to direct laser heating. This information is not easily obtainable from experiments alone, and hence it is considered an important contribution from our numerical modeling. The final melt pool shape is determined by the convection patterns resulting in an asymmetric weld pool as also observed in experiments. In this simulation, we have used the same value of efficiency of laser absorption for both the metals, and hence the observed asymmetry in the melt pool is entirely due to difference in thermal transport properties of the two metals. We have also run simulations using differential laser absorption efficiencies for the two metals, but the effect is found less significant.

3.4 Comparison with Experimental Results

Our computational studies have been performed for the case of stationary spot welding. An asymmetric shift of the Cu-Ni weld pool is shown in Fig. 5. For comparison, corresponding spot welding experiments have also been performed. This is shown in Fig. 8, and a good qualitative agreement of the weld pool shift is found. Variation of mass fraction of copper across the weld pool on the top has been computed and plotted as shown in Fig. 9a. This agrees well with the corresponding experimental results shown in Fig. 9b. The agreement is primarily on the general trend of composition variation. However, the composition curve obtained from computation appears to be smoother, which can be attributed to the assumption of local homogeneity in our mixture model.

The physical processes that take place during laser surface alloying are similar to those during laser welding of dissimilar metals. Heating, melting, mixing of different species and subsequent solidification processes are similar in both the configurations. The process parameters and the directionality of the fluxes are different. However, the compositional variation is to a smaller extent in laser surface alloying as the powder feed rate is usually low. An analysis of the

experiments in this configuration will thus be helpful to gain insight in to the microstructural evolution during solidification of a melt of dissimilar metals. Computational modeling also bears the same similarity with the initial and boundary conditions differing while the governing parameters remain same. In this section, we describe salient features of laser surface alloying experiments and the results of computational modeling.

4. Laser surface alloying Experiments

Laser surface alloying allows synthesis of intermetallic coatings and compositional gradient materials on the surface for better surface properties [20,21,22]. The process typically consists of a moving laser beam with a constant scanning speed in the horizontal direction over a substrate, a thin layer of which melts and forms a pool due to laser heating. Simultaneously, a powder of a different material is fed into the pool, which then mixes with the molten substrate by convection and diffusion. As the laser surface moves away from a location where the pool is already developed, resolidification of the zone occurs leading to a final microstructure of the alloyed surface.

4.1 Experimental Results:

Laser surface alloying experiments were performed with combinations of structurally important metals such as aluminum, iron, copper and nickel [23,24]. The cross-sections of the alloyed samples were characterized using XRD, optical microscopy, SEM and EDAX.

The microstructure and the composition profile of the alloyed region show features specific to the system. Columnar grains (Al-Fe), dendritic microstructure (Ni-Al) and cellular microstructure (Cu-Fe) are all observed. Figure 10 shows the typical microstructures of the alloyed regions for the systems mentioned above. Microstructural features are a function of laser scan rate for all the systems. With a decrease in scan speed, the microstructure changed from columnar to equi-axed in the Al-Fe system. High scan speed refined the spacing of cellular/dendritic structure for the other systems. Composition profile, however, had a different trend. As depicted in Fig. 11, the composition and the hardness showed a gradual increase towards the top of the alloyed region for systems where a lighter element is alloyed on a heavier base metal. For the inverse case, the peak was observed at the middle of the alloyed region. We have extended our computational model for welding to apply for the configuration of surface alloying. The governing equations remain same except the initial and boundary conditions for species equations.

5. Modeling of laser surface alloying

Since this is a moving heat source problem, laser surface alloying is best studied in a coordinate frame that is fixed to the laser source. In such a case, the governing differential equations have to be modified according to an appropriate transformation law, leading to the creation of additional term(s) in the transformed governing equation [25]. The boundary conditions for the species equation are given below:

Top surface (under the laser) $$-D\frac{\partial C}{\partial y} = \dot{q} \qquad 14]$$

Fusion front: $$(1-k)vC = -D\frac{\partial C}{\partial x} \qquad [15]$$

Solidification front: $$vC = -D\frac{\partial C}{\partial x} \qquad [16]$$

In the above expressions, D is the mass diffusivity, C is the concentration, v is the velocity of the front along laser scan (x) direction and k is the partition coefficient.

We have carried out numerical simulation for several traverse speeds and feed rates. A typical numerical result is shown in Fig. 12, which depicts the calculated temperature, velocity and composition distributions with a traverse speed of $0.017 ms^{-1}$ and feed rate of $0.02\ gs^{-1}$. The alloyed pool shape, size and composition distributions show a good qualitative agreement with the corresponding experimental results. The calculated composition gradient at the bottom of the pool is sharp, as observed by composition profile that shows solid solution at the top of the alloy pool. However, the aspect ratio of the computed alloyed pool is slightly larger than the corresponding experimental one. We attribute this difference to the uncertainty of some of the inputs (such as laser coupling efficiency, surface tension coefficient, etc.) to our computational model.

6. Conclusions

Laser welding of dissimilar materials consisting of copper-nickel, iron-copper and iron-nickel has been studied both experimentally and numerically. The experimental observations reveal several complex features of dissimilar metal welding. Firstly, there is an asymmetry in the melt pool shape about the centerline of the butt weld even when the heat source is placed symmetrically on either side. Secondly, there is a large difference in microstructural features between the two sides of the metal-weld interface. The higher conductivity metal side has a smooth interface while the other side has a jagged one. Thirdly, in spite of high convection in the melt pool, the weld has inhomogeneity of composition and microstructure, as revealed by the banding. A preliminary attempt has been made to computationally model this complex phenomenon. In spite of some simplifying assumptions, the model is able to capture some of the key features of the process observed experimentally. This work lays a strong foundation for future studies on the complex issues in dissimilar joints.

Microstructure evolution during laser surface alloying of systems such as iron-aluminium, copper-iron, nickel-aluminium have been studied. The microstructure and hardness of the alloyed region are dependent on the laser scan rate. A numerical simulation of the process is able to predict the shape and size of the pool along with temperature, velocity and composition distributions. Some of the trends suggest a good qualitative agreement with the experimental results.

A computational model to solve heat, momentum and species conservation equations has been developed to provide insights in to the process. Good qualitative agreement between experiments and computation has been achieved. A more complete model requires non-equilibrium solidification to be coupled with heat transfer, fluid flow and species conservation equations.

7. References

1. W.Duley, *Laser Welding of Metals,* John Wiley & sons, New York (1999).
2. W. M. Steen, *Laser Processing of Materials,* Springer-Verlag, London (1991).
3. Z. Sun and J.C. Ion, *Journal of Materials Science*, vol. 30, (1995), p. 4205-4214.
4. G. Metzger and R. Lison, *Welding Journal*, vol. 55, (1976), p. 230s-240s.
5. C. L. Chan, J. Mazumder and M. M. Chen, *Metallurgical Transactions*, vol. 15A, (1984), p. 2175-2184.
6. Y. Joshi, P. Dutta, P. E Schupp and D. Espinosa, *Transactions of the ASME*, vol. 119, (1997), p. 164-172.
7. P.S. Mohanty and J. Mazumder, *Metallurgical Transactions*, vol. 29B, (1999), p. 1269-1279.
8. T. Debroy and S. A. David, *Reviews of Modern Physics*, vol. 67, (1995), p. 85-112.
9. G. Phanikumar, K. Chattopadhyay, and P. Dutta, *Mathematical Modelling of Weld Phenomena*, vol. V, Institute of Metals, (2000).
10. F. K. Chung and P.S. Wei, *Journal of Heat Transfer,* vol. 121, (1999), p. 451-461.
11. Eric A. Brandes, *Smithells Metals Reference Book*, Sixth Edition, Butterworths & Co Publications Ltd., London, (1983).
12. J.C. Ion, H. R. Shercliff, and M. F. Ashby, *Acta Metallurgica et Materialia*, vol.40, (1992), p. 1539-1551.
13. M. Gremaud, M. Carrard and W. Kurz, *Acta Metallurgica et Materialia*, vol. 39, (1995) p. 1431-1443.
14. B. Majumdar, R. Galun, A. Weisheit and B. L. Mordike, *Journal of Materials Science*, vol. 32, (1997), p. 6191-6200.
15. J. Seretsky and E.R. Ryba, 1976, *Welding Journal*, vol. 55, (1976), p. 208s-211s.
16. G. Phanikumar, P. Dutta and K. Chattopadhyay, *Current Science,* vol. 78, (2000), p.847.
17. A. D. Brent, V. R. Voller, and K. J. Reid, *Numerical Heat Transfer*, vol. 13, (1988), p 297-318.
18. S. Chakraborty, G. Phanikumar, P. Dutta, and K. Chattopadhyay, Proceedings, 4th ASME/ISHMT Heat and Mass Transfer Conference, Pune, India, Jan. 12-14, 2000.
19. S. V. Patankar, *Numerical Heat transfer and fluid Flow*, Second Edition, Hemisphere Publications, New York, (1980).
20. I. Manna, J. D. Majumdar, U. K. Chatterjee & A. K. Nath, *Scripta Materialia*, vol. 35, (1996), p. 405.
21. X. He, B. Mordike, N. Pirch and W. Kreutz, *Lasers in Engineering*, vol. 4, (1995), p. 291.
22. Bahadur, O. N. Mohanty, *Journal of Materials Science*, vol. 26, (1991), p. 2685.
23. K.K. Prashant, K. Chatopadhyay and J. Majumder, *Journal of Materials Science,* vol. 34, (1999), p. 3437-3445.
24. G. Phanikumar et. al., vol. 11, Proceedings of EUROMAT '99, Wiley-VCH, Berlin (2000).
25. P. Dutta, Y. Joshi, and R. Janaswamy, Numerical Heat Transfer A, vol. 27, (1995), p. 499 - 518.

TABLE -1. Physical properties of metals used for dissimilar welding

Property	Copper	Nickel	Iron
Melting Point (^{o}C)	1083	1453	1536
Thermal Conductivity ($Wm^{-1}K^{-1}$)	399	88.5	78.2
Specific Heat ($JKgK^{-1}$)	386	452	456
Density (Kgm^{-3})	8900	7905	7870
Latent Heat ($kJmol^{-1}$)	13.02	17.16	15.2

LIST OF FIGURES:

Figure 1. Schematic of Laser Processing setups. (a) welding (b) surface alloying

Figure 2. Typical weld microstructures of Cu-Ni, Cu-Fe and Fe-Ni at low scan speed (a, b, and c) and high scan speed (d, e, and f) respectively.

Figure 3. Interface microstructures of Cu-Ni, Cu-Fe and Fe-Ni (a,b; c,d; and e,f) respectively.

Figure 4. Microstructural bands in Cu-Ni, Cu-Fe and Fe-Ni (a, b, and c) respectively.

Figure 5. Temperature contours of computed Cu-Ni weld pool.

Figure 6. Velocity patterns of computed Cuc-Ni weld pool.

Figure 7. Evolution of the weldpool with time :
Temperature contours at (a)0.6ms (c)1.5ms (e)6.5ms and
Velocity patterns at (b)0.6ms (d)1.5ms (f)6.5ms

Figure 8. Top view of Laser spot weld of Cu-Ni

Figure 9. Compostition profile of Cu-Ni spot weld (a) experimental (b) computed.

Figure 10. Typical microstructure of Laser surface alloyed samples (a) Al on Fe (b) Cu on Fe (c) Ni on Al.

Figure 11. Composition and hardness profiles of Laser surface alloyed samples (a) Al on Fe (b) Cu on Fe (c) Ni on Al.

Figure 12. Computed temperature contours of laser surface alloying of Al on Fe.

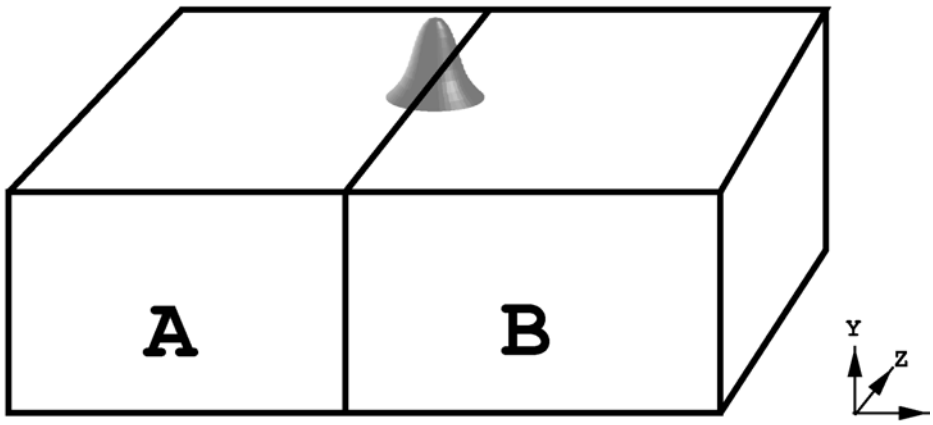

(a)

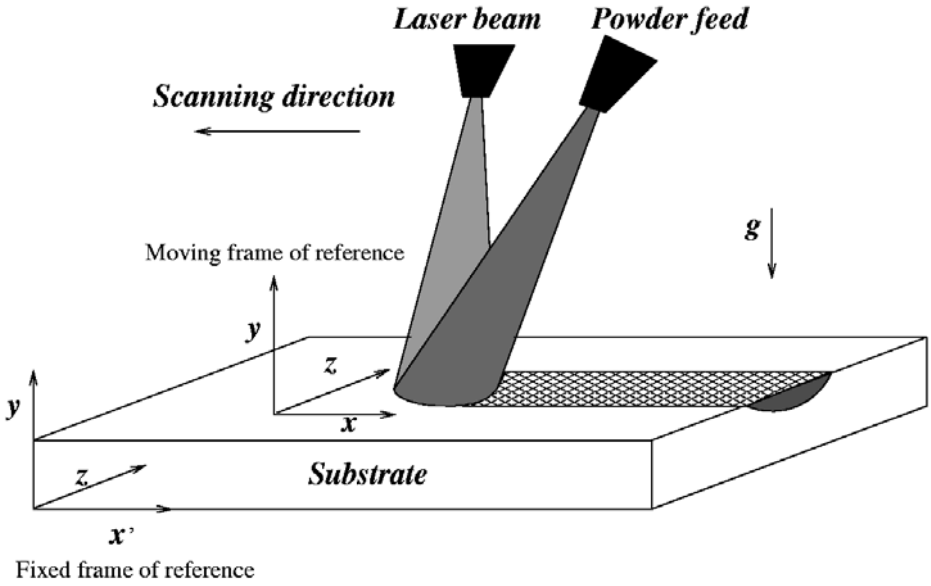

(b)

Figure 1. Schematic of Laser Processing setups. (a) welding (b) surface alloying

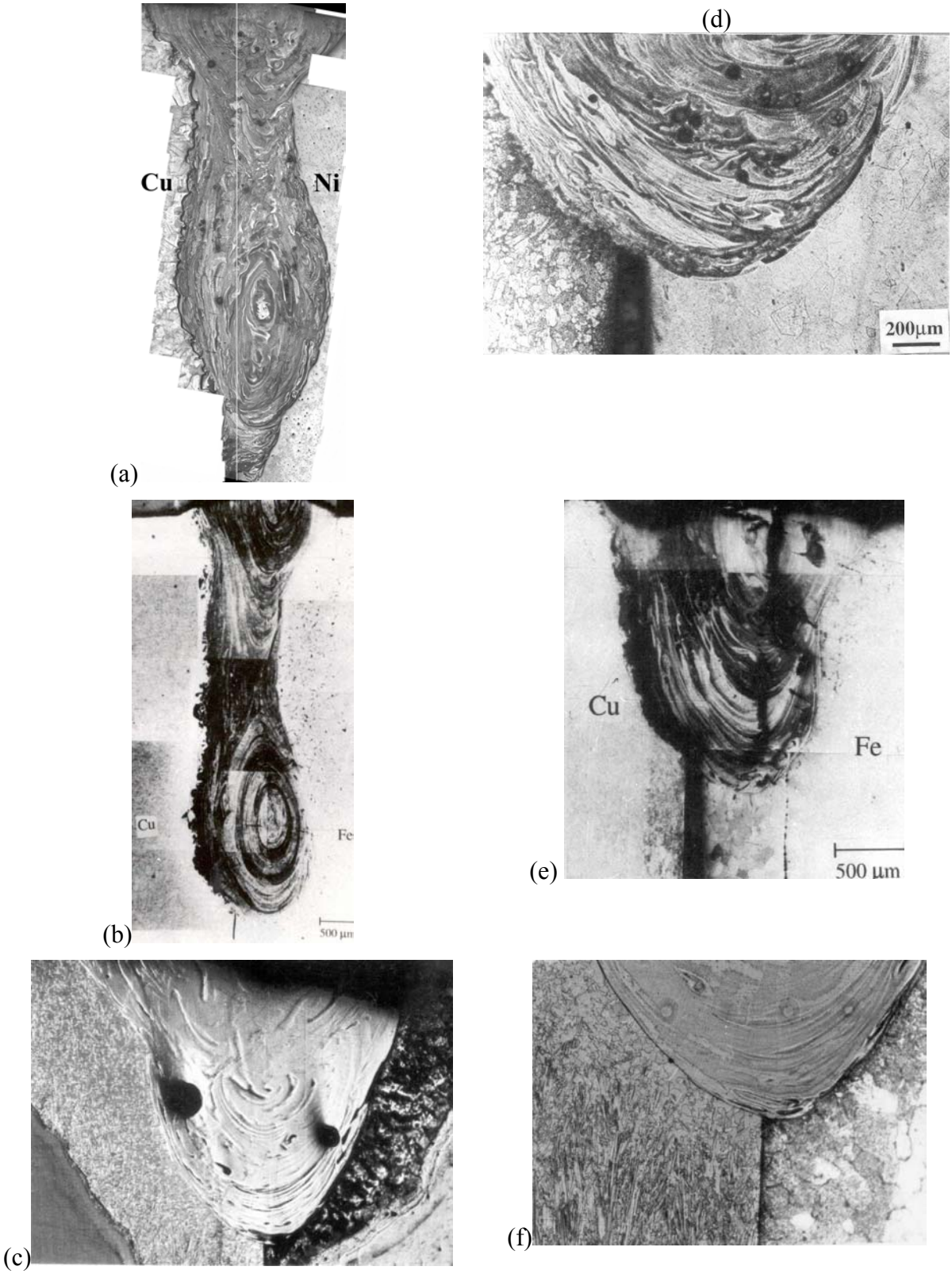

Figure 2. Typical weld microstructures of Cu-Ni, Cu-Fe and Fe-Ni at low scan speed (a, b, and c) and high scan speed (d, e, and f) respectively.

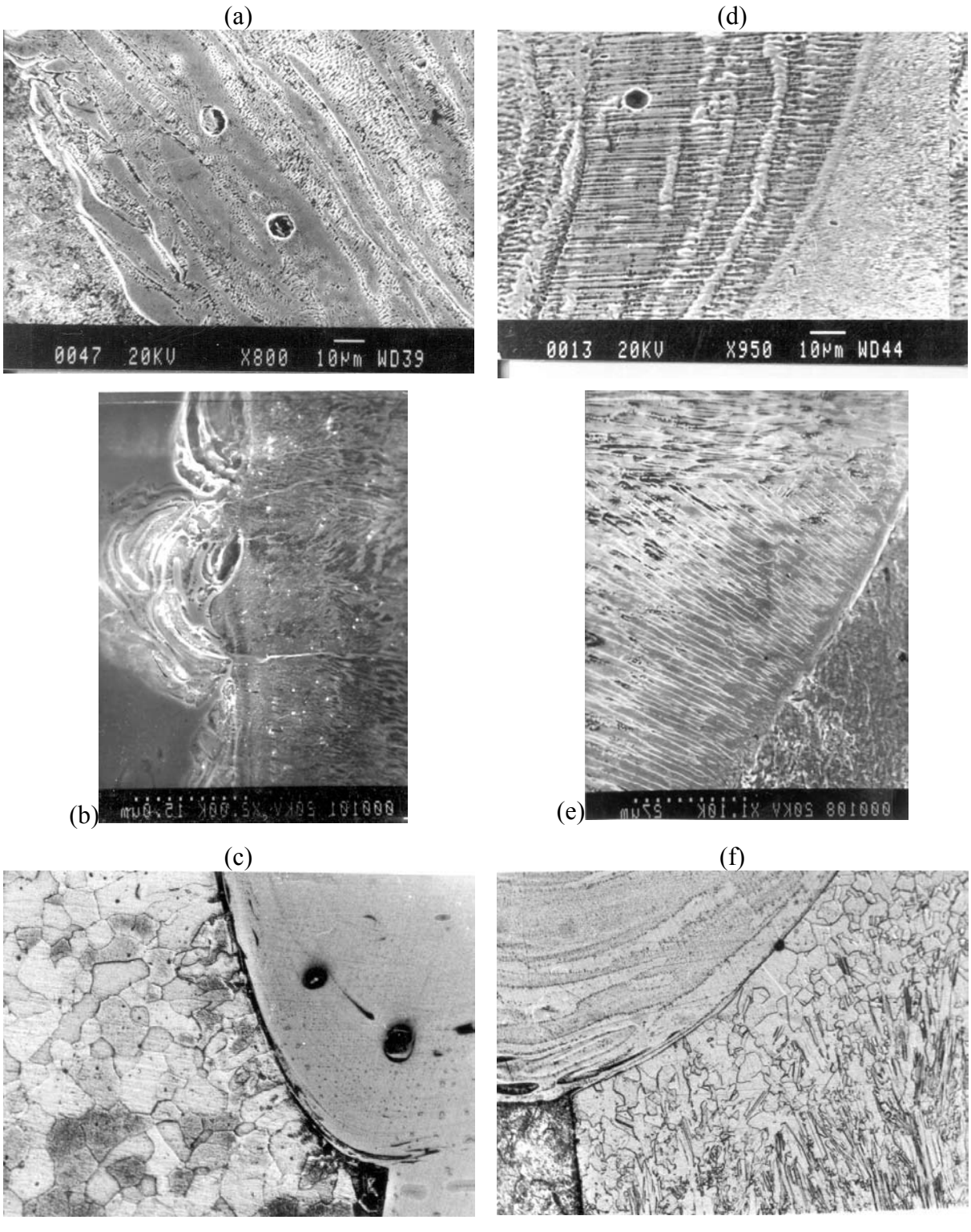

Figure 3. Interface microstructures of Cu-Ni, Cu-Fe and Fe-Ni (a,b; c,d; and e,f) respectively.

(a)

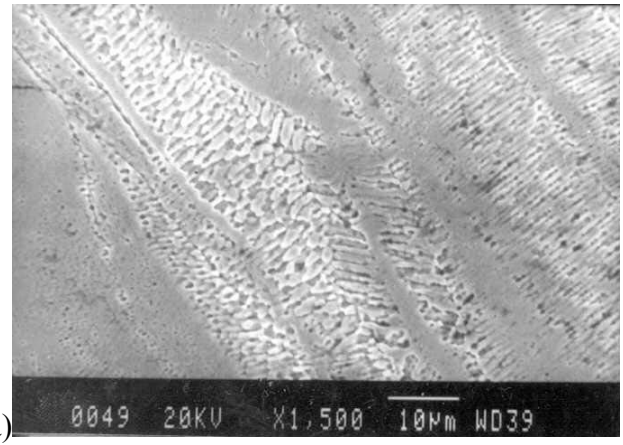

(b)

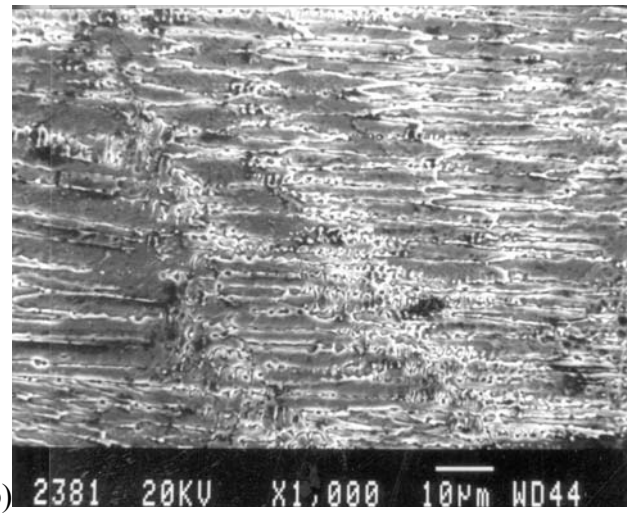

(c)

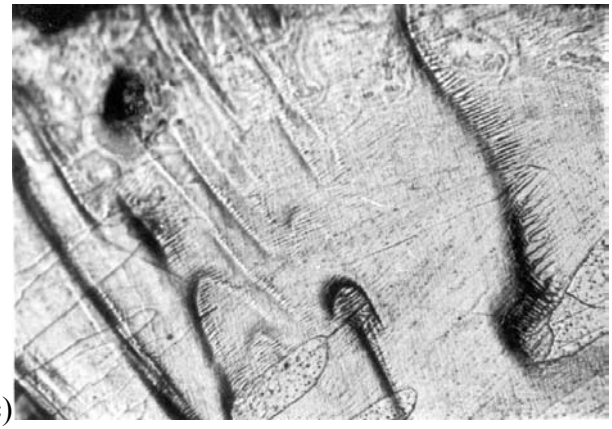

Figure 4. Microstructural bands in Cu-Ni, Cu-Fe and Fe-Ni (a, b, and c) respectively.

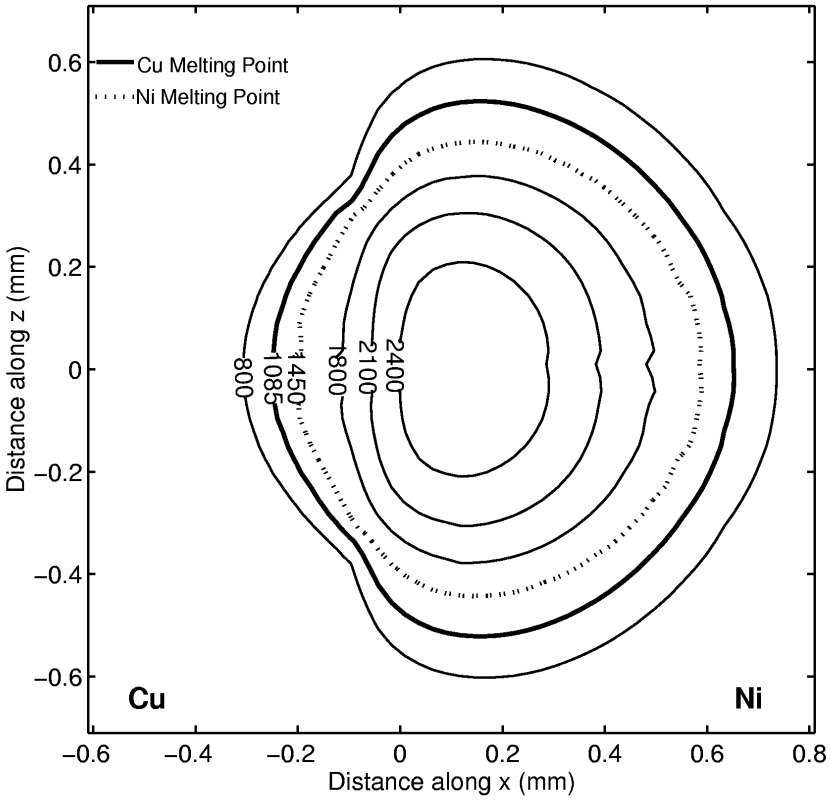

(a)

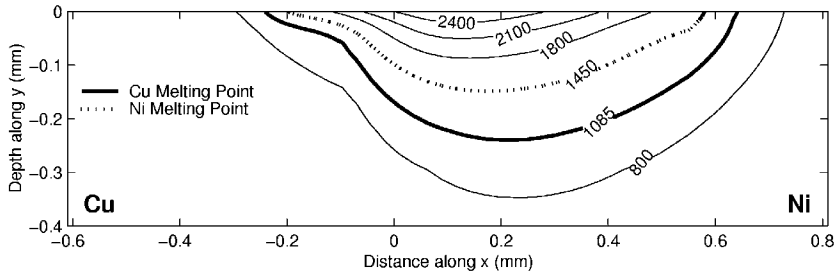

(b)

Figure 5. Temperature contours of computed Cu-Ni weld pool.

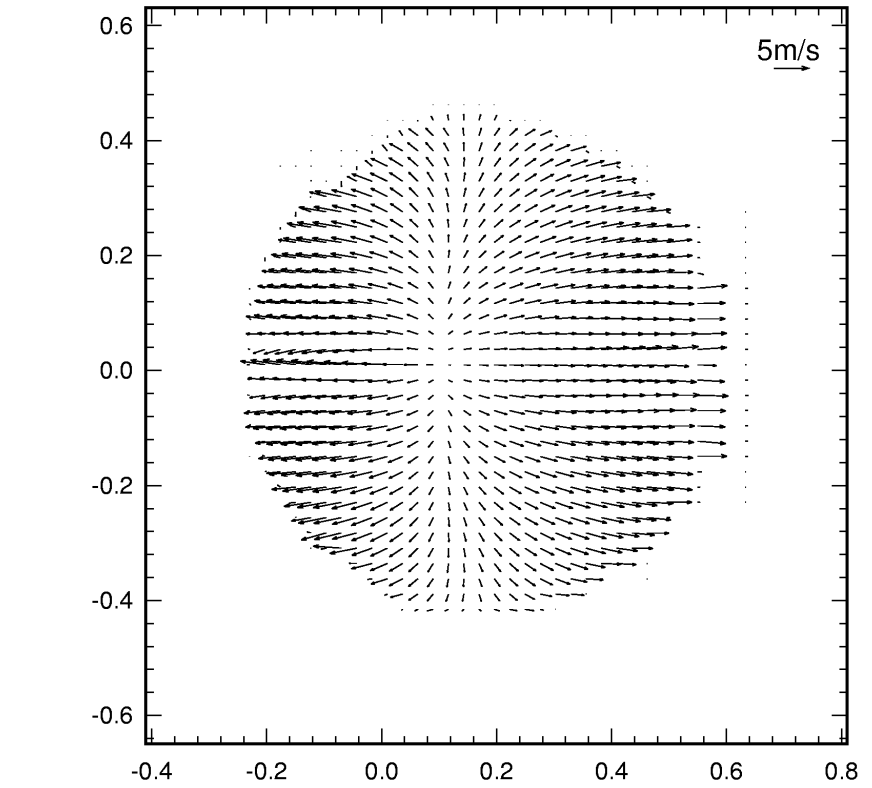

(a)

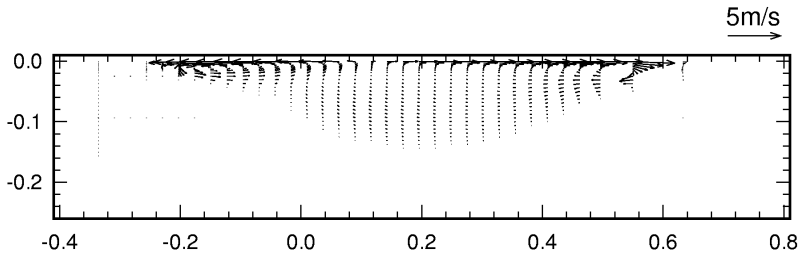

(b)

Figure 6. Velocity patterns of computed Cu-Ni weld pool.

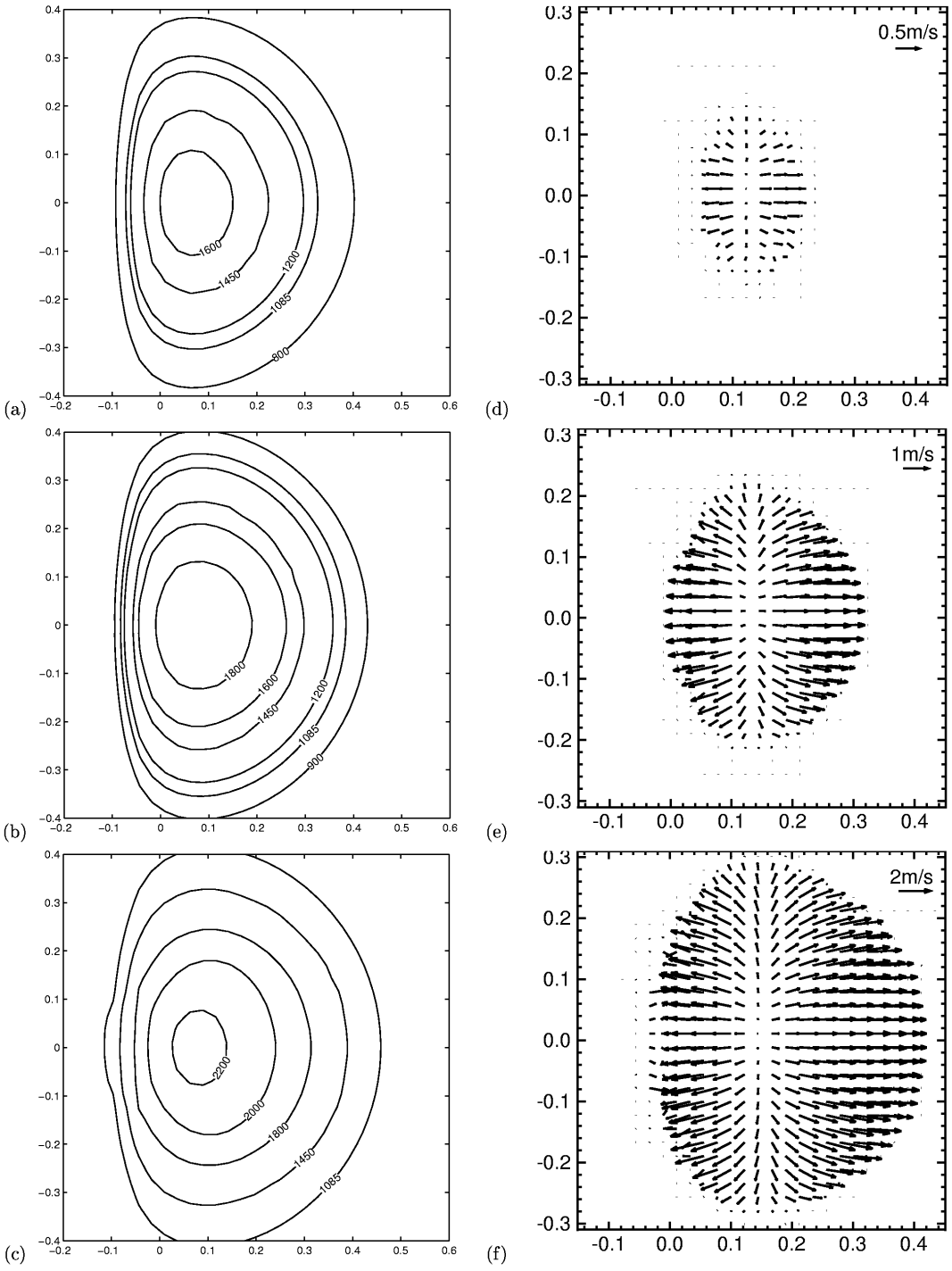

Figure 7. Evolution of the weldpool with time :
Temperature contours at (a)0.6ms (c)1.5ms (e)6.5ms and
Velocity patterns at (b)0.6ms (d)1.5ms (f)6.5ms

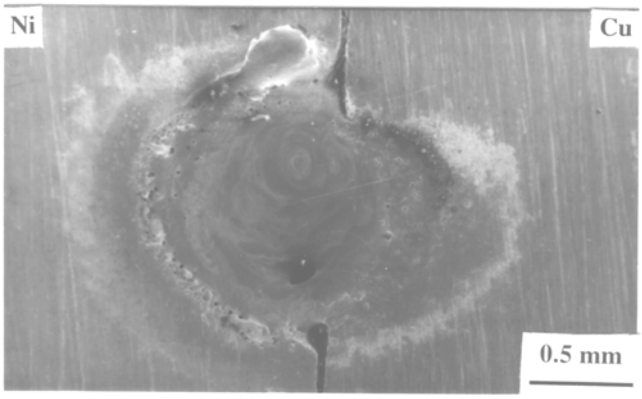

Figure 8. Top view of Laser spot weld of Cu-Ni

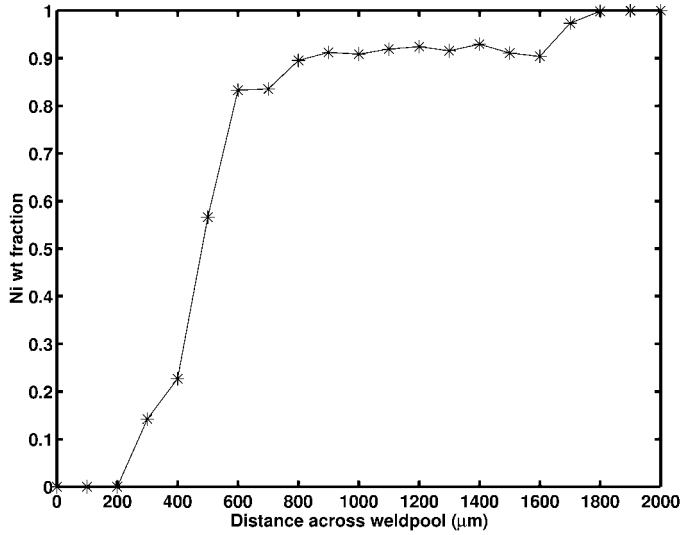

(a)

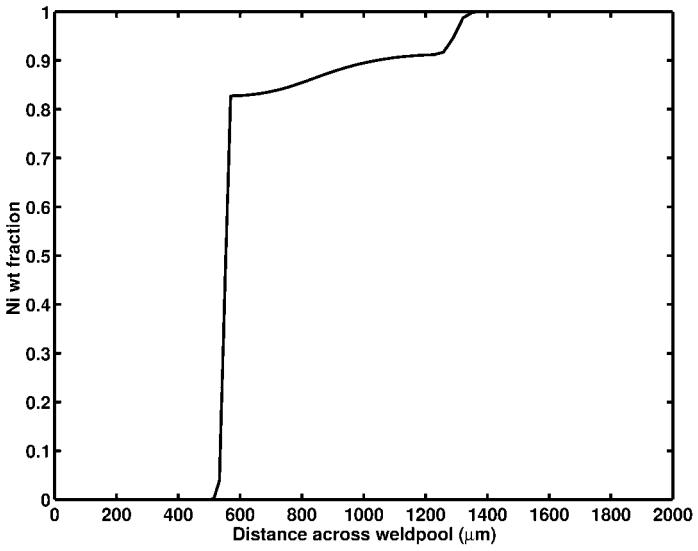

(b)

Figure 9. Compostition profile of Cu-Ni spot weld (a) experimental (b) computed.

(a)

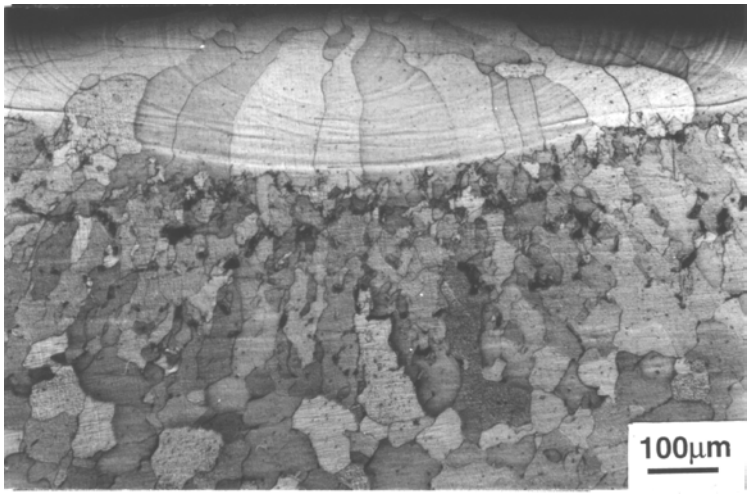

(b)

(c)

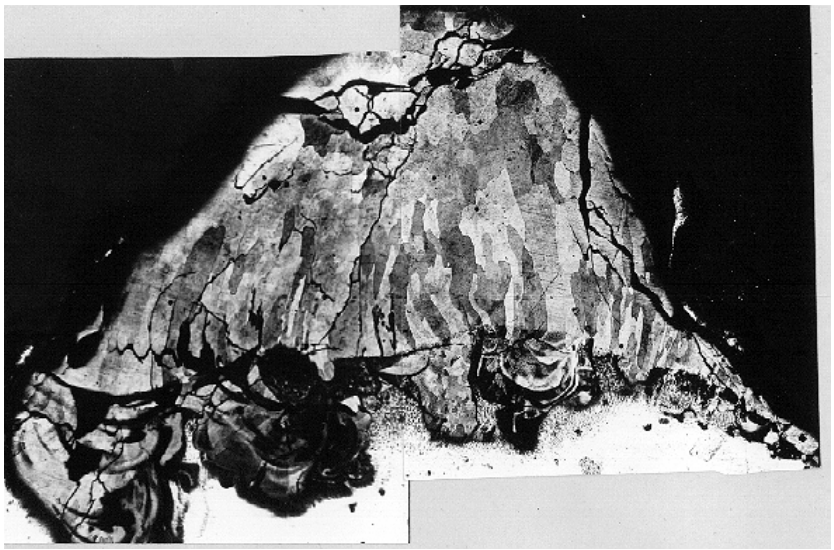

Figure 10. Typical microstructure of Laser surface alloyed samples (a) Al on Fe (b) Cu on Fe (c) Ni on Al.

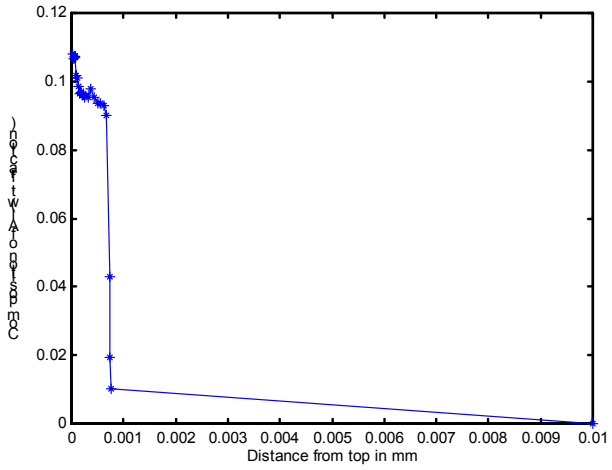

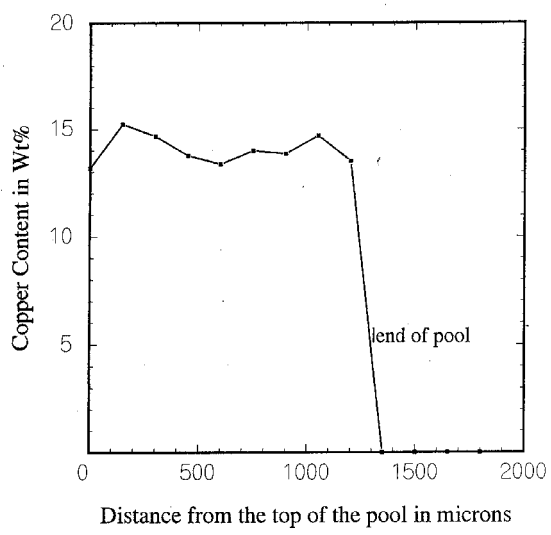

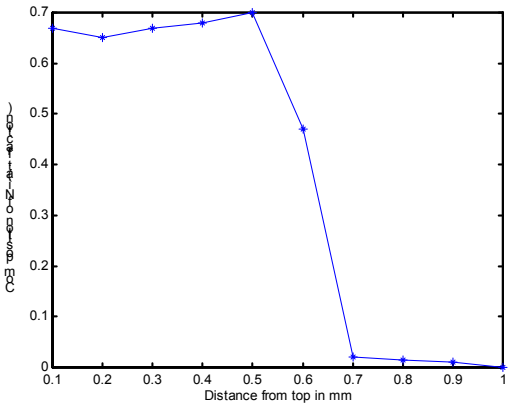

Figure 11. Composition and hardness profiles of Laser surface alloyed samples (a) Al on Fe (b) Cu on Fe (c) Ni on Al.

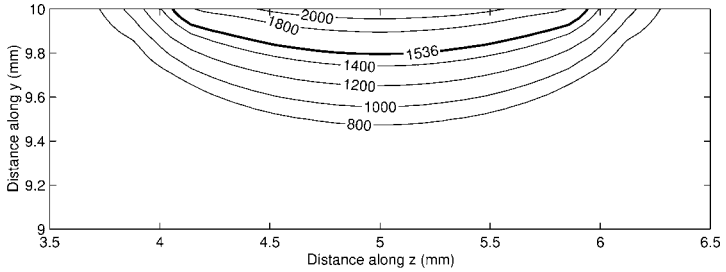

(a)

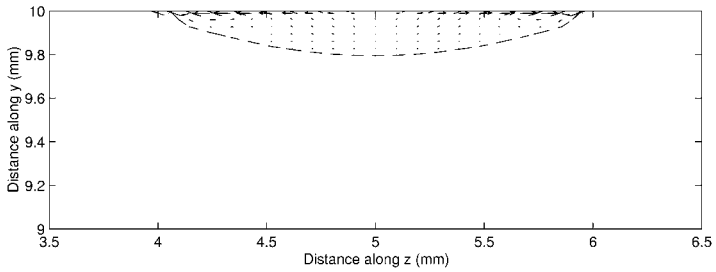

(b)

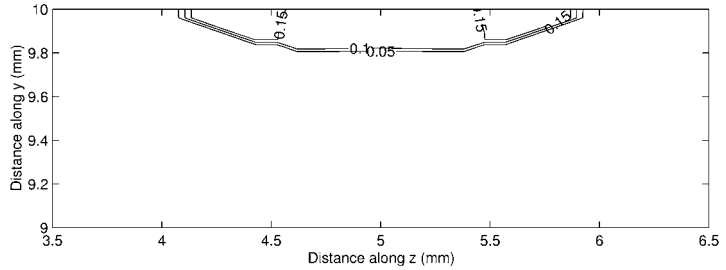

(c)

Figure 12. Computed temperature contours, velocity patterns and composition contours of laser surface alloying of Al on Fe.